Chapter 4

Band-gap tuned hexagonal-Boron Nitride/reduced Graphene Oxide superlattice wrapped Cadmium Sulfide/Polypyrrole nanocomposite as an efficient supercapacitor electrode material

Contents

4.1. Introduction

Recent years have witnessed expeditious exploration and advancement of renewable energy sources caused by the detrimental effects of exhaustion of fossil fuels on the environment. Modern E-devices rely on energy conversion and storage to fulfil the increasing global energy need with long-term sustainability. In this direction, the supercapacitor has gained interest as an energy storage device owing to their superior specific capacitance, large power density, rapid charge-discharge rate, and long cycling stability [1]. Metal sulphides have attracted researchers' interest as a potential material for supercapacitor electrode due to their greater electrical conductivity [2] and more electrochemical activities than that of metal oxides/hydroxides [3]. Moreover, in alkaline electrolyte, metal sulphides exhibit reversible redox reactions (MS + OH– = MSOH + e-, where M = transition metal). The presence of valence states in materials such as CdS, CuS, CoS and NiS improves energy density and demonstrates excellent specific capacitance [4]. Among these sulphides Cadmium Sulfide (CdS) is an outstanding pseudocapacitive material owing to their larger surface area, superior electrical conductivity, cost-effective, low toxicity and environmental stability [5]. Even, nanocomposites of CdS such as WO_3-CdS provide high capacitance with 133% capacitance retention [6]. One-step hydrothermal growth of porous CdS on Ni foam substrate was demonstrated to have a 909 F/g specific capacitance at a current density of 2 mA/cm^2 [7]. However, the theoretical specific capacitance of 1675F/g using CdS electrode is much higher than that obtained experimentally [5]. The electrochemical properties of a CdS-based supercapacitor can be improved in a variety of ways. Using a composite of CdS and EDLC as an electrode material, such as graphene, CNT, and activated carbon, is one technique to boost the performance of supercapacitors [8, 9]. In this direction, Graphene based CdS composite has been extensively studied by researchers owing to its excellent specific capacitance and electrical conductivity, high surface area and great mechanical strength [10-12].

Nowadays, conducting polymers (CP) like polypyrrole (PPy), polyaniline, etc. has been studied in depth for supercapacitor applications due to their better conductivity, rapid charge/discharge mechanism, high thermal stability, low cost and excellent energy density [13]. The main disadvantage of CP is swelling and shrinkage during the charge/discharge processes, resulting in poor cycling stability that severely limits their practical use [13]. Various types of PPy nanostructures combined with GO or rGO nanosheets have been reported to enhance capacitance and improve rate capabilities [14]. The synthesis of these nano-composite sheets are based primarily on the strong attraction of Van der Waals forces between the basal plane of highly aromatic graphene and π conjugated PPy chains [15, 16]. Here rGO nanosheets act

as a conducting framework beneath the PPy layer facilitating the transfer of electrons between rGO and PPy by restricting the swelling and shrinkage of PPy.

The present work reports on the synthesis of h-BN/rGO wrapped CdS/PPy nanocomposite by simple hydrothermal method and in situ oxidative polymerisation process. The h-BN/rGO super-lattice act as a conducting framework and the h-BN/rGO–CdS core-shell structure prevents the swelling and shrinking of CdS nanoparticles thus providing more electrochemical activity and stability. The strong π-π bond between rGO sheets and PPy chain can prevent the PPy deformation caused by expansion and contraction, thereby, improving the cyclic stability [17]. The synergetic effect of high capacity metal sulphide, highly stable h-BN/rGO superlattice framework and high conducting, porous PPy polymer backbone has been exploited in this work to develop an efficient electrode material for supercapacitor applications.

4.2. Experimental section

Materials and chemicals

Graphite flakes, Nitric Acid (70%), Sulfuric acid (98%), $KMnO_4$, H_2O_2 (30%), HCl (37%), h-Boron Nitride, Cadmium Sulfide, L-Ascorbic Acid, $FeCl_3.6H_2O$, Methyl Orange, Pyrrole monomer were bought from Merck and Sigma-Aldrich. All the reagents used were of analytical quality and were utilised as delivered.

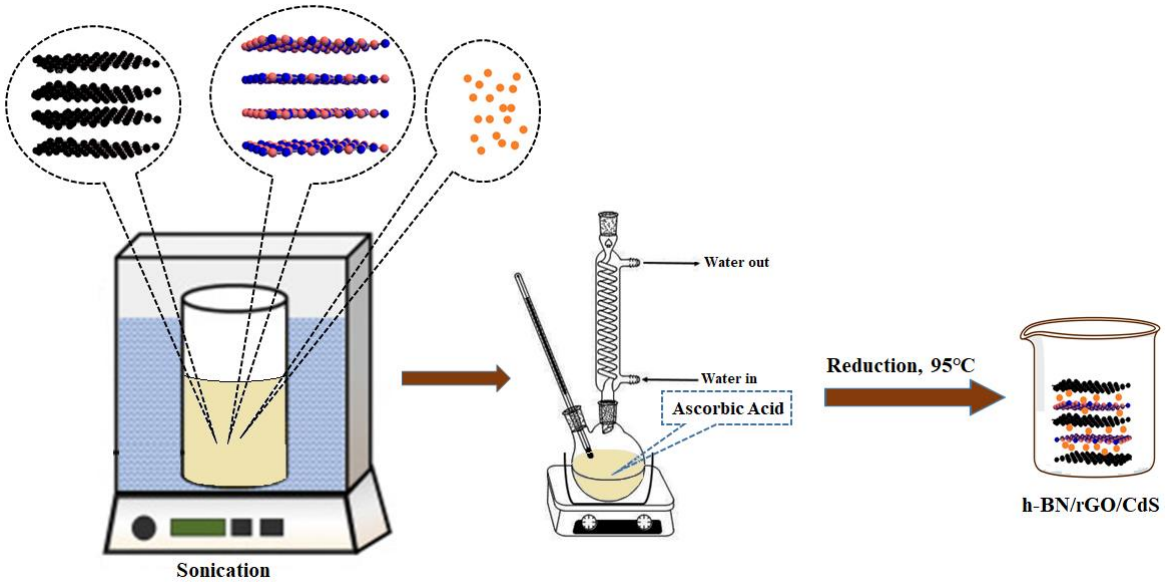

Fig.4.1. Hydrothermal process for the preparation of h-BN/rGO/CdS nanocomposite

Preparation of h-BN/rGO/CdS nanocomposite

For the synthesis of GO, modified Hummers method was employed [10]. 50mg of h-BN was mixed with 2-Propanol and sonicated for 3h and the supernatant was separated. A 50mg of GO was introduced into DI water and sonicated for 3h (Fig.4.1). Then, 200mg CdS was mixed to the solution and further sonicated for 30mins. Both the solutions were mixed together and 500mg of L-Ascorbic acid was dissolved into the mixture and refluxed at 95℃ for 12h. The resulting sample was filtered, washed thoroughly with DI water and dried. For comparative analysis, rGO/CdS and h-BN/rGO samples were synthesized using same method and without the addition of h-BN and CdS respectively.

Preparation of h-BN/rGO/CdS@PPy

To prepare h-BN/rGO/CdS@PPy composite, firstly, h-BN/rGO/CdS sample was dispersed in 25ml DI water. Then, 1M HCl was dropped slowly into the solution followed by 2.5mM of Methyl Orange. Subsequently, 50mM pyrrole monomer was introduced into the prepared mixture and the solution was stirred for some time in an ice bath (Fig.4.2). After that, 50mM

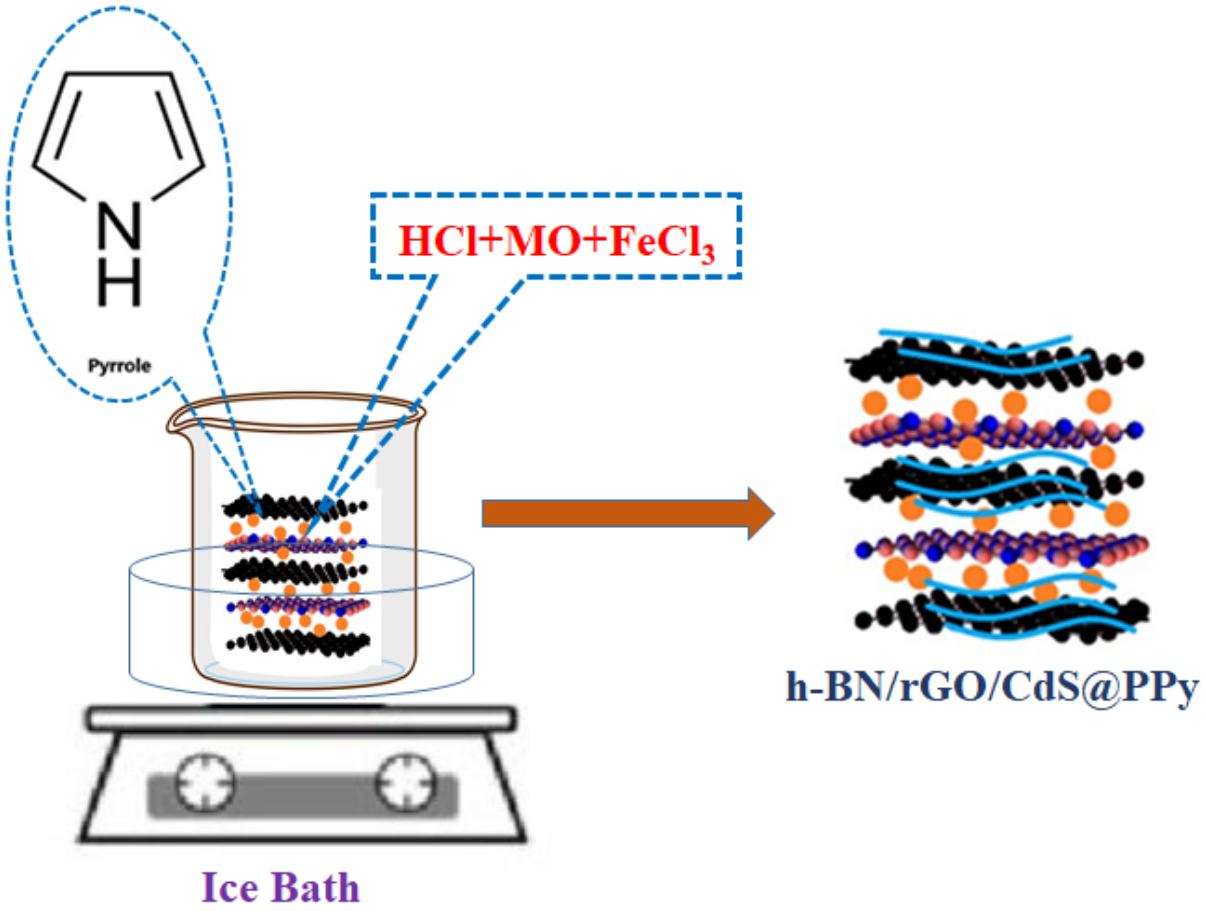

Fig.4.2. Chemical oxidative polymerisation for the preparation of h-BN/rGO/CdS@PPy

$FeCl_3$ was slowly introduced into the mixture under stirring for polymerisation. After stirring for 5h at a temperature of 0-5°C, the mixture was filtered, washed and dried in a vacuum oven. It was named h-BN/rGO/CdS@PPy. The PPy was synthesized by using same procedure and without the addition of h-BN/rGO/CdS.

Electrode preparation method

The fabrication of working electrode was done by adding a mixture of synthesized nanocomposite (80%), carbon black (10%) and PVDF binder (10%) to NMP solvent under sonication to obtain the slurry. The prepared slurry was coated on a cleaned ITO glass by using drop-casting method and dried in a vacuum oven at 70 ℃. The mass loading of the active material is ~1.2mg.

Characterization Methods

Fourier transform infrared spectroscopy (FTIR) was recorded to identify the functional groups contained in present in the h-BN/rGO/CdS@PPy composite material using a Nicolet Impact 410 FTIR spectrophotometer. The crystalline nature and interlayer spacing of the composite was recorded by powder X-ray diffraction (XRD) (Bruker AXS D8FOCUS) using Cu-Kα radiation where λ = 1.540598 Å, scan rate of 1˚/min. The graphitization degree along with defects present in the samples was studied by Raman spectroscopy (Renishaw Basis Series with 514 Lasers). UV–Vis spectroscopy was recorded using (Thermo Scientific UV-10 Spectrometer). Surface area (Brunauer-Emmett-Teller) and pore size distribution were recorded in NOVA 1000E, NOVA WIN, QUANTACHROME. Prior to adsorption/desorption tests, the sample was degassed at 150°C for 8 hours to remove moisture and atmospheric vapours using heat and evacuation. The morphology study was performed using Transmission Electron Microscopic (TEM) (TECNAI G2 20 S-TWIN (200 kV)). The Autolab PGSTAT128 Potentiostat/Galvanostat electrochemical workstation was employed to analyze the electrochemical characteristics of samples. The cyclic voltammetry (CV) measurements were carried out in a voltage range of 0-0.6 V using 3M KOH solution with Platinum as counter electrode and Ag/AgCl as reference electrode in a 3-electrode system at varying scan rates. The Galvanostatic Charge−Discharge (GCD) tests were carried out at various current densities with cut-off voltages of 0V and 0.6V. The Electrochemical Impedance Spectroscopy (EIS) was recorded for 100kHz to 0.1Hz frequency range using 10mV (rms) AC sinusoid signal at open circuit potential.

To evaluate the practical applicability of the nanocomposite, an asymmetric supercapacitor (ASC) was made employing h-BN/rGO/CdS@PPy as positive electrode and activated carbon (AC) as negative electrode. A filter paper soaked in 3M KOH solution served as the separator. CV, GCD and EIS of the device was measured using 2-electrode system.

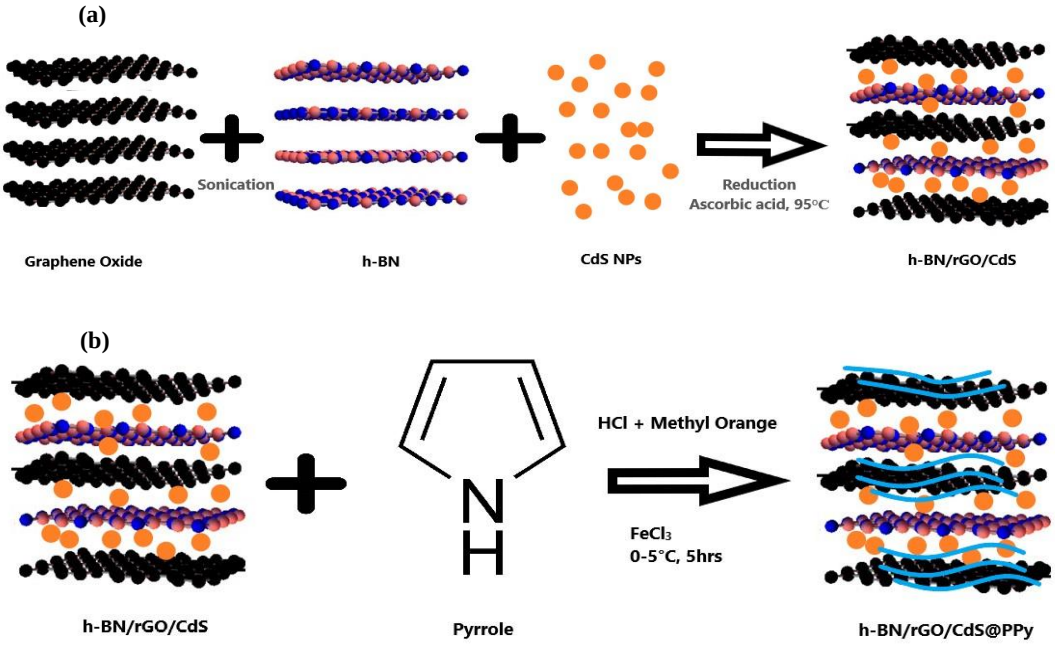

Fig.4.3. Schematic illustration of h-BN/rGO/CdS@PPy synthesis (a) hydrothermal process for the preparation of h-BN/rGO/CdS nanocomposite (b) Chemical oxidative polymerisation for the preparation of h-BN/rGO/CdS@PPy

4.3. Results and Discussion

Reaction for synthesis of h-BN/rGO/CdS@PPy

Fig.4.3 shows synthesis mechanism of h-BN/rGO/CdS@PPy nanocomposite restacking structure. The h-BN/rGO/CdS nanocomposite was synthesised by using hydrothermal process and the h-BN/rGO/CdS@PPy composite was made by h-BN/rGO/CdS composite and PPy sample through oxidative polymerisation. Initially, h-BN and GO were mechanically exfoliated by ultra-sonication. While they reassemble GO sheets and h-BN nanosheets tend to stack alternatively forming a superlattice structure with much lower band-gap energy [18]. Here the wedging-in of h-BN nanosheets in between graphene layers prevents the agglomeration of rGO layers. The restacking of rGO layers in between h-BN sheets lowers the offset Fermi level [19]. As a result, there is a lowering of band-gap in h-BN/rGO superlattice promoting fast transfer of electrons in the nanocomposite through formation of conducting framework. Further, the

introduction of CdS nanoparticles (NPs) while restacking of h-BN and rGO nanosheets, entraps the CdS NPs in between the sheets forming a core-shell like structure (Fig.4.3a). The core-shell structure of h-BN/rGO – CdS inhibits the volume change of CdS NPs, thus, enhancing its cycling stability. The similar band-gaps of h-BN/rGO (2.5eV) and CdS (2.40eV) enhances effective inter-charge transfer mechanism. Further nanocompositing of h- BN/rGO/CdS with highly conductive and porous PPy increases the electrochemical activity providing easy conducting routes for charge transfer (Fig.4.3b).

Characterization

From FTIR spectra, the wide peak at 3425cm^{-1} in Fig.4.4a represents bending vibrations of (-OH) group as well as residual water moieties in the samples [10]. The peaks in 2922cm^{-1} and 2855cm^{-1} attributes to C–H stretching peaks showing the existence of C-H groups in all samples except h-BN sample [20]. In h-BN sample, the peak at 810cm^{-1} and 1368cm^{-1} attributes to B–N–B out-of-plane bending vibration and B–N in-plane stretching vibrations [21]. The presence of the above peaks are also appeared more prominent in the final sample (h-BN/rGO/CdS@PPy) confirming the formation of h-BN nanosheets [22]. In PPy sample, peaks at 1540cm^{-1} denotes ring stretching vibrations of C=C bond and 1450cm^{-1} attributes to ring's C–N/C–C stretching modes [23]. Also, the peaks at 3425cm^{-1} and 1285cm^{-1} represent N-H stretching vibration and C-N stretching vibrations, respectively [24]. The C–H out of the plane ring deformation vibrations (905cm^{-1} and 778cm^{-1}) as well as C-H in-plane deformation vibration (1025cm^{-1}) are also noticed in PPy sample [25, 26]. The weak band at 602cm^{-1} attributes to Cd-S bond's stretching demonstrating the existence of CdS in the sample and the

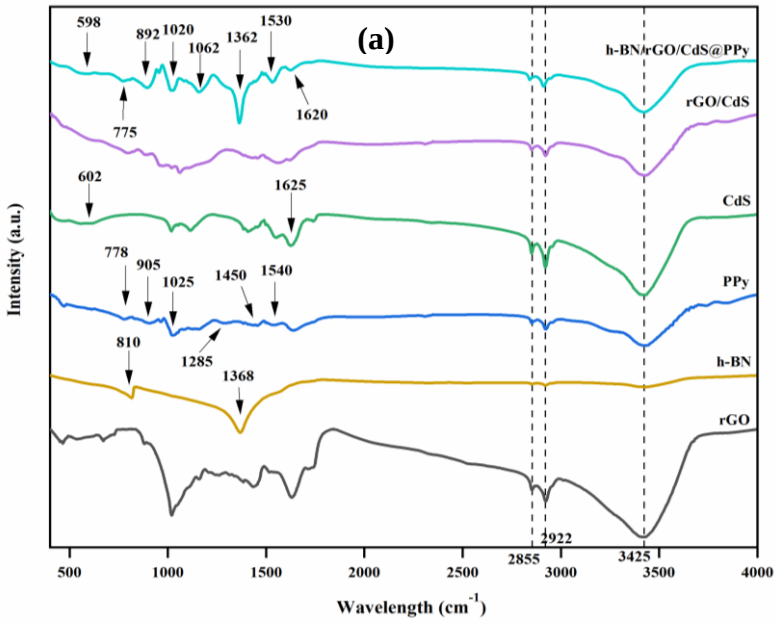

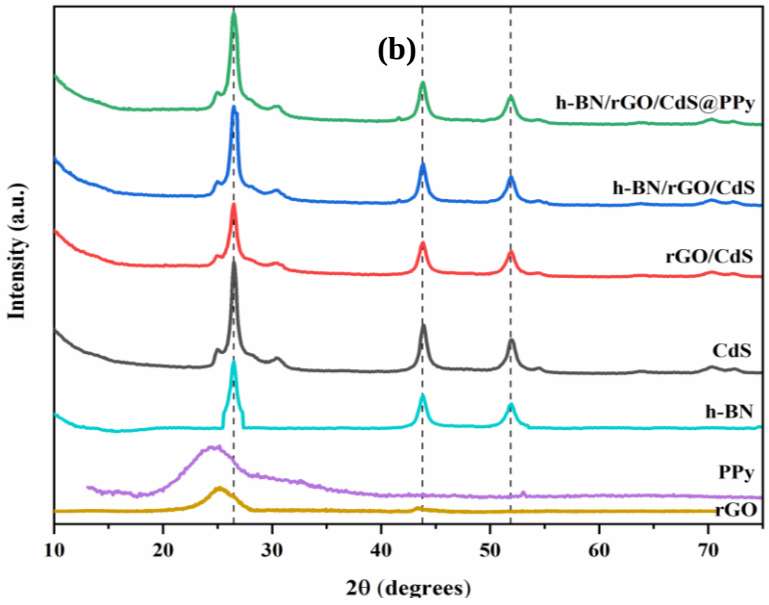
(b)
h-BN/rGO/CdS@PPy
h-BN/rGO/CdS
rGO/CdS
CdS
h-BN
PPy
rGO
Intensity (a.u.)
10
20
30
40
50
60
70
2θ (degrees)

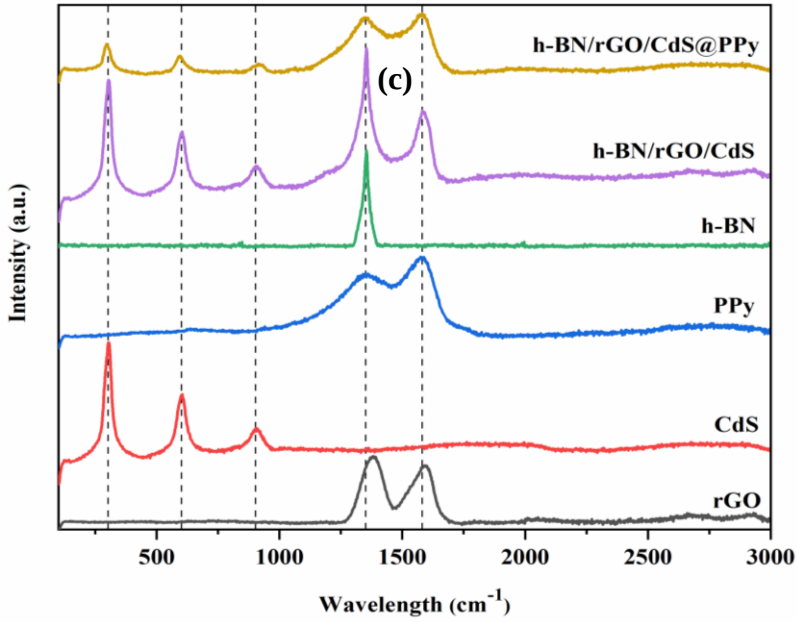
(c)
h-BN/rGO/CdS@PPy
h-BN/rGO/CdS
h-BN
PPy
CdS
rGO
Intensity (a.u.)
500
1000
1500
2000
2500
3000
Wavelength (cm-1)

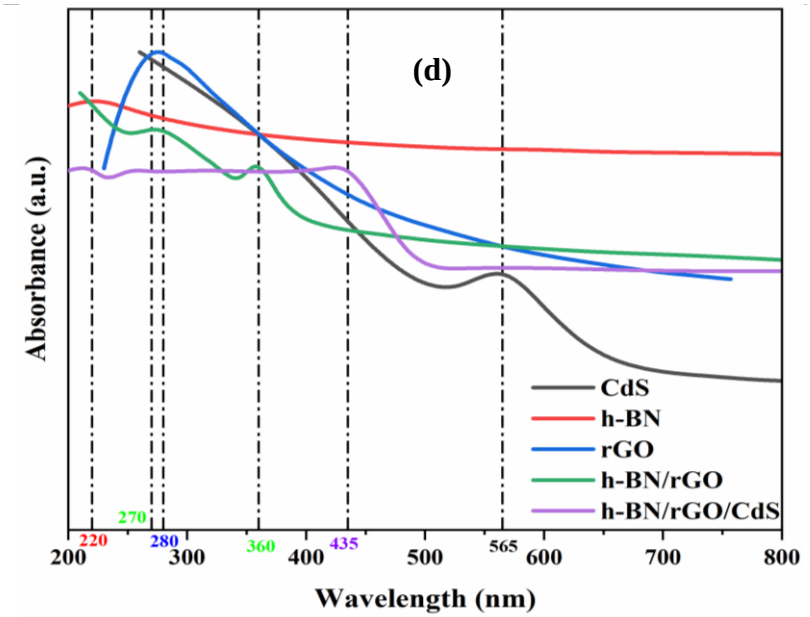
(d)
CdS
h-BN
rGO
h-BN/rGO
h-BN/rGO/CdS
Absorbance (a.u.)
220
270
280
360
435
565
200
300
400
500
600
700
800
Wavelength (nm)

Fig.4.4. Characterization of samples (a) FTIR spectra of rGO, h-BN, PPy, CdS, rGO/CdS, h-BN/rGO/CdS@PPy (b) XRD patterns of rGO, PPy, h-BN, CdS, rGO/CdS, h-BN/rGO/CdS, h-BN/rGO/CdS@PPy (c) Raman spectra of rGO, CdS, PPy, h-BN, h-BN/rGO/CdS, h-BN/rGO/CdS@PPy (d) UV spectra of CdS,h-BN, rGO, h-BN/rGO, h-BN/rGO/CdS

weak intensity peak is obtained due to the existence of moisture in the sample [27]. The weak peak also has arisen at 1625cm^{-1} due to CdS stretching [28]. In final h-BN/rGO/CdS@PPy sample, all the above peaks are appeared with a slight shift towards smaller wave number indicating the bonding of the dopants into the h-BN/rGO superlattice during h-BN/rGO/CdS@PPy nanocomposite's synthesis [29].

XRD pattern in Fig.4.4b shows peaks corresponding to crystal planes of the synthesized rGO, PPy, h-BN, CdS, rGO/CdS, h-BN/rGO/CdS and h-BN/rGO/CdS@PPy. The peak at 2θ =24.5° and 42.5° indicate the reflection from (002) and (100) plane of the rGO sample with d=0.36nm respectively [30]. For the h-BN sample, the reflection peak at 2θ = 26° (d=0.34nm) attributes to (002) plane and weaker reflections at 2θ=43.7° and 52° corresponds to (100) plane and (102) planes respectively [31, 32]. The similarity in crystal plane orientation in rGO and h-BN sample confirms same graphitic like honey comb structure in h-BN sample. In XRD spectra of CdS sample, the peaks at 26°, 44° and 52° corresponds to the reflection from (002), (110) and (112) planes respectively [33, 34]. The typical diffraction peak of rGO at 2θ=26° was shielded by the strong characteristic peak of CdS at 2θ=25.5° in the rGO/CdS sample. Similarly, the diffraction peak of h-BN and PPy are also effectively shielded in the composites with CdS owing to its relatively low diffraction intensity in the superlattice. The crystallinity of all composites was identical to that of pure CdS, suggesting that the crystallinity of CdS is preserved after the nucleation process.

The Raman spectra in Fig.4.4c shows two prominent peaks (D and G) of each sample - for rGO at 1590cm^{-1} and 1383cm^{-1}, h-BN/rGO/CdS at 1581cm^{-1} and 1353cm^{-1} and h-BN/rGO/CdS@PPy at 1581cm^{-1} and 1351cm^{-1} respectively. The degree of disorder is defined by D band whereas the G band gives information about the inherited graphitic domain [30]. The h-BN/rGO/CdS@PPy sample showed the peak broadening and shifting of the D band and G band to slightly lower wave number, indicating an increase in disorder driven by the wedging-in of nanoparticles into few-layer reduced graphene nano-sheet stacks [35]. The

characteristic peak at around 303cm^{-1}, 604cm^{-1} and 903cm^{-1} are attributed to CdS NPs' first (1LO), second order (2LO) and third overtone (3LO) of the longitudinal optical phonon vibrational modes [36]. The sharp peak at 1353cm^{-1} is associated with the in-plane E2g phonon mode of h-BN [37]. From the spectra of PPy, C=C backbone stretching at 1351cm^{-1} and ring-stretching mode of PPy are observed at 1581cm^{-1} respectively. However, there are no clear bands of rGO or h-BN detected in the plot of h-BN/rGO/CdS@PPy composite implying PPy and CdS are not just mixed up or blended with rGO/h-BN, instead PPy and CdS are entrapped in the h-BN/rGO framework [38]. The characteristic band of rGO/h-BN disappeared because of the strong interaction between CdS/PPy and rGO/h-BN. Hence, Raman spectrum of h-BN/rGO/CdS@PPy confirms the successful integration of CdS and PPy into the h-BN/rGO superlattice [39].

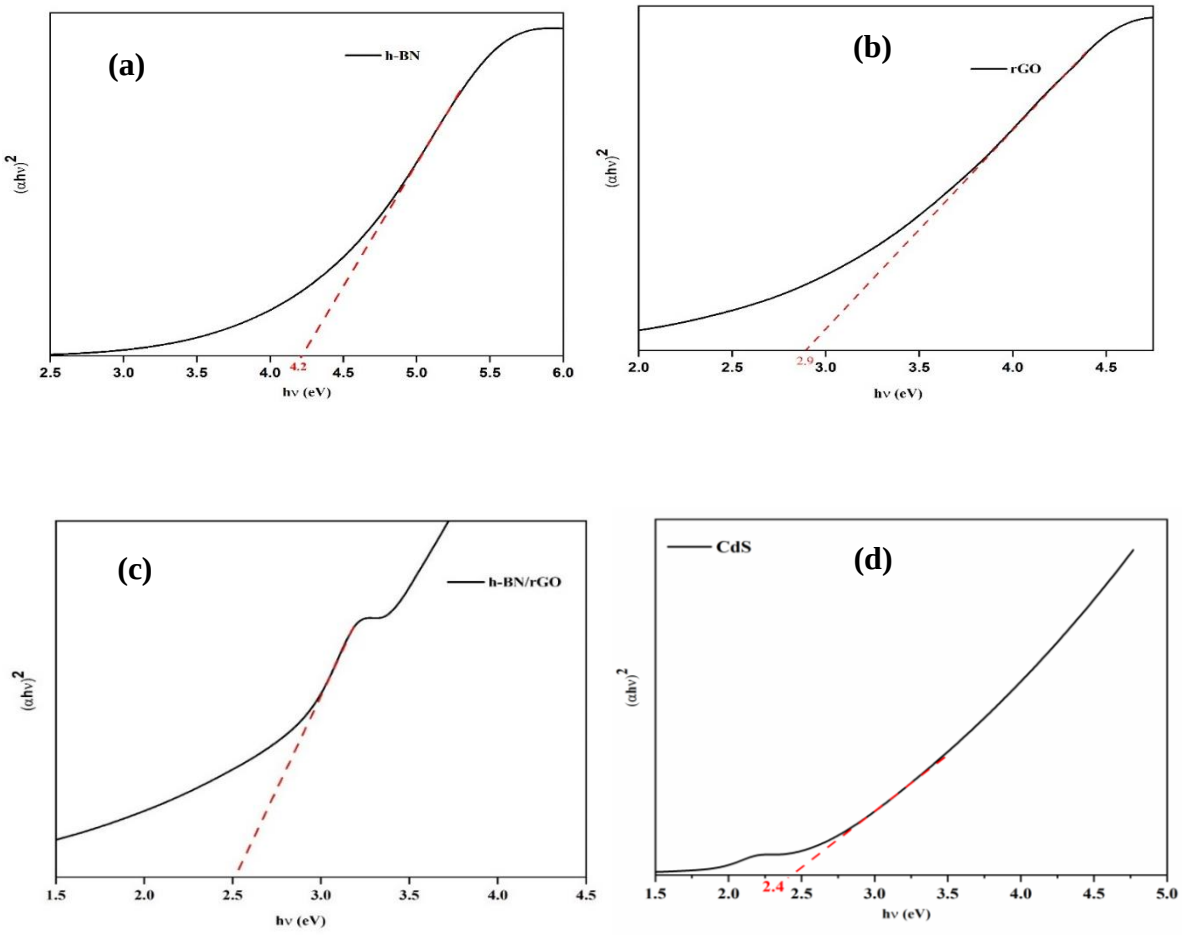

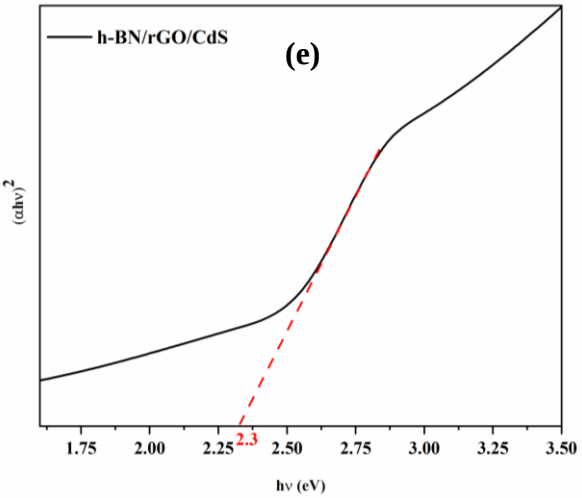

Fig.4.5. Tauc plot (a) h-BN (b) rGO (c) h-BN/rGO (d) CdS (e) h-BN/rGO/CdS

To determine the optical and electronic characteristics of samples, UV-visible spectroscopic characterization of the h-BN/rGO superlattice (Fig.4.4d) was conducted. An absorption peak for h-BN was observed at 220nm which corresponds to 4.2eV band-gap energy estimated from Tauc plot of h–BN sample (Fig.4.5a) [40, 41]. The interaction of electron-hole in the π-π* transition of aromatic C-C bonds in graphitic domain provides the absorption peak of rGO at 280nm [30]. The energy band-gap of rGO is calculated to be 2.9eV (Fig.4.5b). There are two peaks seen in UV spectra of h-BN/rGO nanocomposite at 270nm and 360nm. The peak at 270nm is seen in between that of pure h-BN and rGO implying that graphene layers are inserted in between h-BN layers (Fig.4.2), thus, forming h-BN/rGO superlattice [42]. The h-BN and graphene domains are large enough to help in the retention of their individual bandgap identities, as evidenced by the presence of two distinct absorption peaks, effectively forming a superlattice rather than a substitution doped (B and N in C) or alloyed phase between h-BN and graphene [42]. The estimated band gap of h-BN/rGO is 2.5eV from Tauc plot (Fig.4.5c). The reduced band-gap of h-BN/rGO superlattice than that of pristine rGO is attributed to the prevention of agglomeration while restacking of graphene nanosheets and also modification of band structure by the alternate stacking of h-BN sheets [18, 19, 43]. The successful formation of superlattice with a lower energy-gap will increase the electrical conductivity of the composite and also serves as a conducting framework for enhanced electrochemical performance. The CdS NPs showed a peak at 565nm [44] which corresponds to a bandgap of 2.40eV (Fig.4.5d). The h-BN/rGO/CdS NPs showed a peak at 435nm which corresponds to a bandgap of 2.30eV (Fig.4.5e).

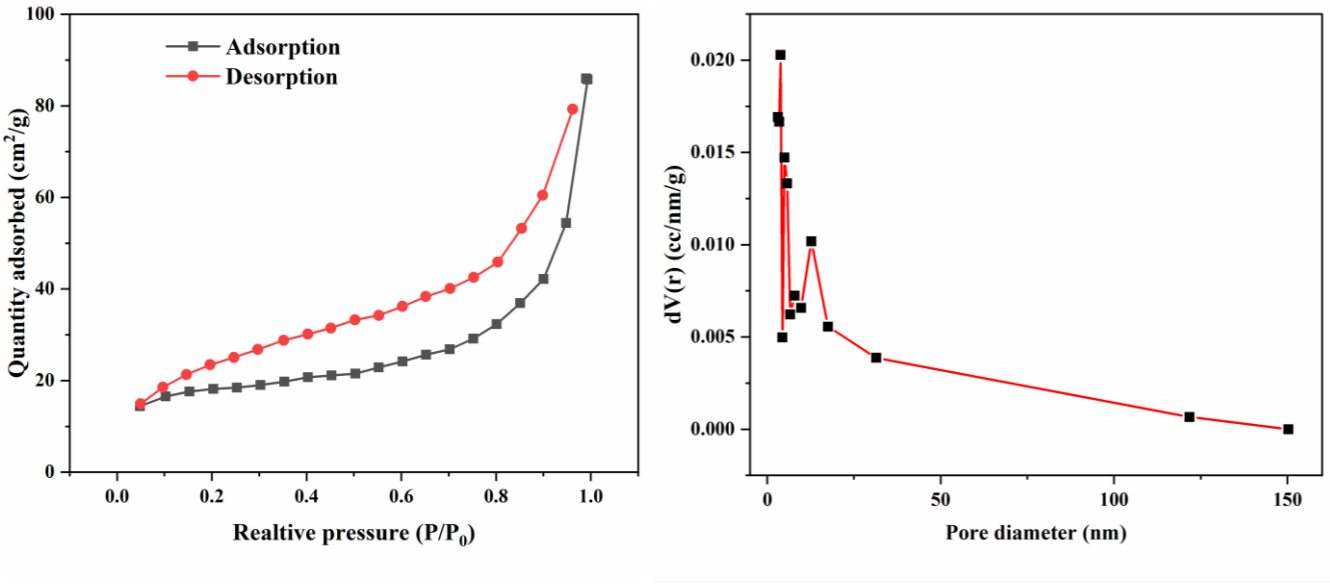

Fig.4.6 (a) N2 adsorption/desorption isotherms of h-BN/rGO/CdS@PPy. (b) Pore size distribution of h-BN/rGO/CdS@PPy.

In the N_2 adsorption-desorption isotherm of h-BN/rGO/CdS@PPy (Fig.4.6a), adsorption hysteresis loop can be seen in the middle area and a curve can be seen in the latter section which are typical type-IV isotherm characteristics [45]. The BET surface area, pore volume and pore size were determined as 267m^2/g, 0.17cc/g and 3.85nm respectively. From the pore size distribution graph (Fig.4.6b), pores are mostly distributed in the range 3-32nm confirming its mesoporous nature. Also, macropores at around 121nm was recorded [46].

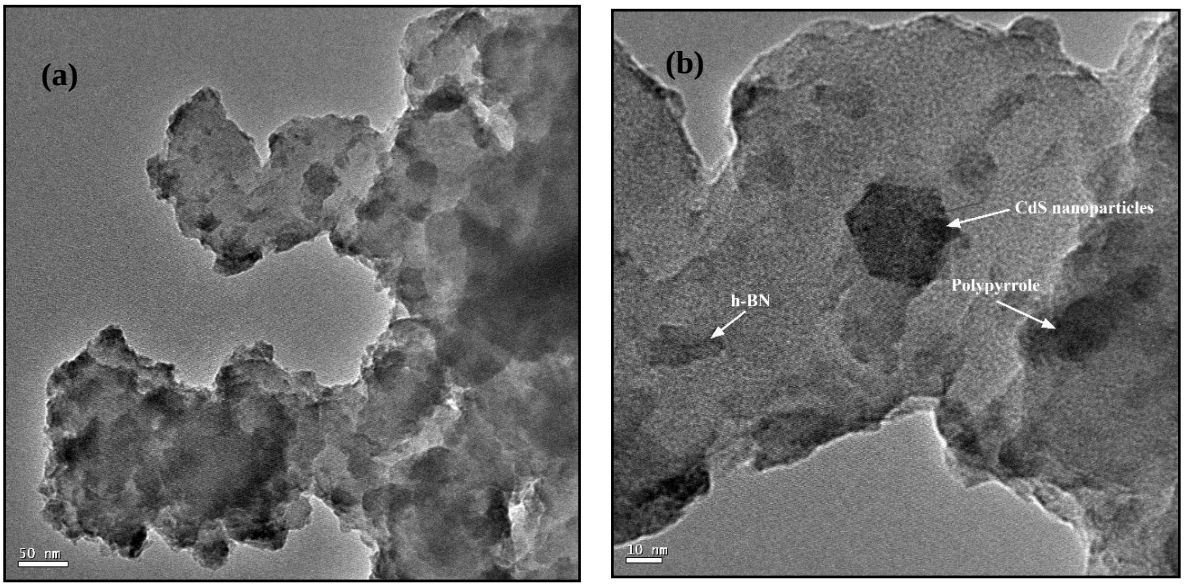

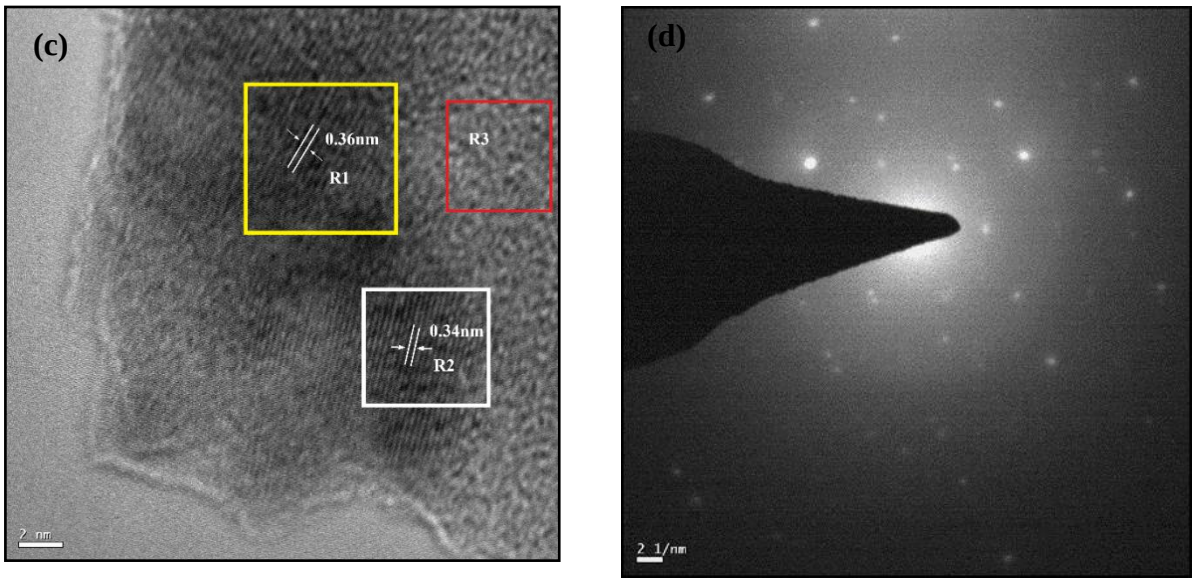

Fig.4.7 Electron microscopic morphology : a) TEM of h-BN/rGO/CdS@PPy (b) Magnified TEM of h-BN/rGO/CdS@PPy (c) HRTEM of h-BN/rGO (d) SAED pattern of h-BN/rGO

The TEM image analysis was employed to investigate the morphology of the sample. The TEM image in Fig.4.7a presents the morphology of h-BN/rGO/CdS@PPy sample revealing the formation of nano-composite. The magnified TEM image in Fig.4.7b shows CdS nanoparticles and PPy nanosheets embedded on the h-BN/rGO sheet. The wurtazite hexagonal structures of CdS nanoparticle with a diameter of 35nm is clearly seen and wrapped inside the h-BN/rGO sheets. The polypyrrole sheets seen in the image closely resembles the nano sheets synthesized by previously reported literature [34]. For further morphology study of h-BN/rGO structure, the HRTEM image has been performed presenting 3 regions (R1, R2 and R3) highlighted in Fig.4.7c. The lattice space of 0.36nm in R1 region corresponds to the (002) plane of rGO nanosheets matching well with the XRD results [30]. The lattice space of 0.34nm in R2 region corresponds to the (002) plane of h-BN domain matching well with that of h-BN [47]. The distortion of lattice structure in R3 region is ascribed to the existence of rGO component in the h-BN/rGO moiety as well as the increasing defect as a result of decreased sp2 hybridisation [48]. This result confirms repetitive growth of graphene layers in between h-BN layers and the formation h-BN/rGO superlattice. The SAED pattern in Fig.4.7d indicates circled diffraction pattern corresponding to the above crystal planes of the crystalline regions in the nanocomposite sample.

Electrochemical analysis

The cyclic voltammetry measurements of CdS, rGO/CdS, h-BN/rGO/CdS and h-BN/rGO/CdS@PPy were performed in 3M KOH aqueous electrolyte at several scan rates by maintaining the potential window of range 0-0.6V used to prevent over oxidation of PPy [49]. The CV analysis of the nanocomposites performed at 20mV/s (Fig.4.8a) shows quasi-rectangular shaped curves implying the capacitive behaviour owing to the integrated effect of faradaic as well as non-faradaic reactions [50-52]. Here, CdS, h-BN and PPy contributes faradaic reactions and rGO exhibits EDLC properties [13, 53]. The cyclic voltammogram of all the samples reveals that h-BN/rGO/CdS@PPy nanocomposite has the greatest current response and largest area exhibiting more specific capacitance than that of other samples. The difference in the oxidation state of B and N provides auxiliary pseudo capacitance through chemi-adsorption of hydroxyl (-OH) groups in alkaline medium due to the distinction in the electronegativities between B,C and N atoms (2.0, 2.5 and 3.0 respectively) [48]. The separate phase is formed within the nano dimension contributing C-C and B-N bonds' stability and will also aid in the π-conjugation [54]. The incorporation of rGO into h-BN lattice lowers band gap with enhanced electron density of conduction layer exhibiting charge transfer through electrolyte redox reaction [40]. A proper overlapping of π-π orbitals of CPs and h-BN/rGO superlattice accelerates the movement of electrons between individual components resulting better current response and stability of composite electrodes. Moreover, non-hierarchical assembly of h-BN/rGO superlattice structure improves the electrochemical characteristics [55]. Fig.4.8b shows the CV of h-BN/rGO/CdS@PPy at different scan rates. The inability of the protons and alkali cations to get enough time for deep penetration into the layers of the materials at high scan rates resulted in the charge built-up at the interface leading to the deviation of CV plots from the ideal rectangular shape [56]. In addition, the electrolyte ions' diffusion helps in gaining penetration to the electrode's available surface area before any complete insertion reaction at low scan rate, giving a superior specific capacitance (Cs) [57-59]. As the scan rate increased, the CV curves for h-BN/rGO/CdS@PPy retains their shapes (Fig.4.8b), indicating better capacitive behaviour, reversibility and electrochemical stability of the fabricated electrode.

Fig.4.8c compares the GCD curves of all samples from 0-0.6 V vs. Ag/AgCl at 1 A/g. From the GCD plots, an obvious departure from the triangular shape could be seen for all the samples, suggesting that the capacitance of the fabricated electrodes is primarily caused by reversible faradic redox reactions [60, 61]. The electrode material has internal resistance (iR drop) causing voltage drop at the initial of the discharge curve. The h-BN/rGO/CdS@PPy

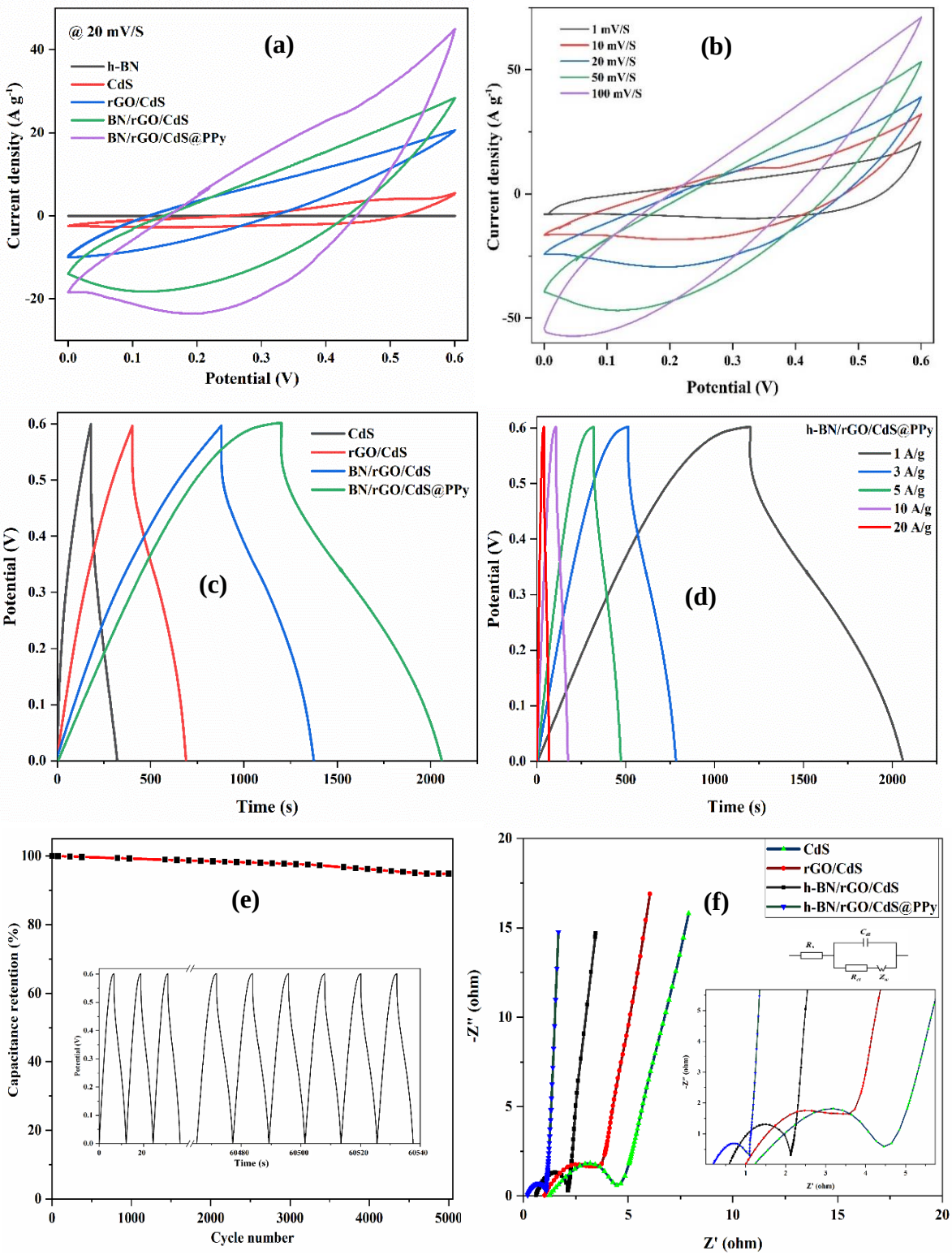

Fig.4.8 (a) CV of all the samples at 20mV/S, (b) CV of h-BN/rGO/CdS@PPy at different scanning rates, (c) GCD of all the samples at 1 A/g, (d) GCD of h-BN/rGO/CdS@PPy at different current densities, (e) Cycling stability of h-BN/rGO/CdS@PPy at a current density of 10 A/g, (f) EIS of all the samples

shows enhanced electrical conductivity with minimum internal resistance as well as minimum iR drop (50 mV) compared to CdS (154 mV), rGO/CdS (100 mV) and h-BN/rGO/CdS (84 mV) as observed in Fig.4.8c. The iR drop measured is in agreement with the Nyquist plots. The specific capacitance of CdS, rGO/CdS, h-BN/rGO/CdS and h-BN/rGO/CdS@PPy was computed from GCD curve as $Cs = \frac{i.\Delta t}{m.\Delta V}$ =240 F/g, 478 F/g, 825 F/g and 1435 F/g respectively at 1 A/g [62-64], where i/m = current density (A/g), Δt =discharge time (s) and ΔV = potential (V). The h-BN/rGO/CdS@PPy sample shows more current density in CV, a prolonged discharge time in GCD and lowest iR drop confirming the superior electrochemical properties of the prepared sample [65-67]. Moreover, the h-BN/rGO/CdS@PPy shows outstanding rate capability and cyclic stability. As current density increases, the specific capacitance drops (Fig.4.8d). It attributes to the surface charge storage process occurring only at higher current densities [68]. Here the doping of carbon decreases the energy gap of insulating h-BN layers through π-conjugation of carbon channel improving its electrical conductivity and electrochemical performance. The near band-gap difference of CdS (2.40eV) and h-BN/rGO superlattice (2.5eV) also promotes the inter charge transfer mechanism thereby enhancing electrical and electrochemical properties of the nanocomposite.

The cycling stability of h-BN/rGO/CdS@PPy sample was tested by GCD for 5000 cycles at a current density of 10A/g. After 5000 cycles, the sample demonstrated remarkable cycling stability with a capacitance retention of 95% (Fig.4.8e). This is owing to the wrapping of h-BN/rGO super-lattice preventing the swelling and shrinking of CdS which resulted in enhanced electrochemical characteristics and stability of the supercapacitor electrode. Also, the strong π-π bond between the rGO sheets and the PPy chain also prevents PPy deformation caused by expansion and contraction thereby improving the cyclic stability.

EIS was conducted to investigate the impact of electrochemical reaction kinetics on improved electrode performance. In the EIS plot, the following 3 regions were observed: the x-intercept at the beginning of the semicircle caused by equivalent series resistance (Rs); the semi-circle in the high frequency zone as a result of charge transfer resistance (Rct), and the nearly vertical straight line in the low frequency zone gives rise to good capacitive behaviour and low diffusion resistance [69-73]. The EIS spectra in Fig.4.8f shows that h-BN/rGO/CdS@PPy nanocomposite has the least series resistance compared to other samples due to the enhanced conduction of electrons through the framework. The Rct values for the CdS, rGO/CdS, h-BN/rGO/CdS and h-BN/rGO/CdS@PPy were around 3.45Ω, 2.90Ω, 1.70Ω and 0.92Ω respectively. From Table.4.1, the Rct of h-BN/rGO/CdS@PPy are smaller than other samples,

suggesting the rapid charge transfer performance of the nanocomposite. Moreover, it is clear from the graph that the slope of h-BN/rGO/CdS@PPy is higher than that of other samples, showing a smaller Warburg resistance [74].

Table 4.1. Electrochemical Impedance properties of h-BN/rGO/CdS@PPy

Sample	Rs (Ω)	Rct (Ω)	Zw ($m\Omega/s^{0.5}$)
CdS	1.25	3.45	0.45
rGO/CdS	1.01	2.90	0.38
h-BN/rGO/CdS	0.60	1.70	0.11
h-BN/rGO/CdS@PPy	0.20	0.92	0.07

The near band-gap difference of h-BN/rGO (2.5 eV) superlattice and CdS (2.40 eV) aids in the fast intra charge transfer mechanism. In addition, the chemical synthesis route of PPy were optimized to achieve high conductivity and specific surface area by fixing methyl orange concentration (2.5 mM) and polymerization temperature (0-5˚C) [75, 76]. Also, the porous nanostructure of PPy efficiently improves supercapacitors' capacitance, as they feature high surface area accompanied with enhanced electroactive sites that ease and speed up electrolyte ions' diffusion into the electrode's interior parts. The lower impedance of h-BN/rGO/CdS@PPy nanocomposite is attributable to the enhanced conductivity due to low band-gap h-BN/rGO superlattice and porous PPy, promotes electron transport into the composite electrode, rendering it an appropriate choice for supercapacitors.

An asymmetric supercapacitor was made using h-BN/rGO/CdS@PPy as the positive electrode and activated carbon as the negative electrode in order to examine the practical applicability of the nanocomposite. Fig.4.9a presents the CV of ASC at scan rates from 1mV/s to 100mV/s in a voltage window of 0 – 1.5V. It was seen that when the scan rate increased, all curves took a similar shape, indicating the device has excellent fast-charge/discharge capabilities [77]. Fig.4.9b presents the GCD curves of ASC at various current densities and the maximum specific capacitance was computed as 102F/g at a current density of 1A/g. With the current density increased to 30A/g (Fig.4.9c), the ASC still maintained a specific capacitance of 76F/g that is 74.5% of that at 1A/g. The smaller semicircle in the high frequency zone of Nyquist plot (Fig.4.9d) and the almost perpendicular line in the low frequency zone indicate a low charge

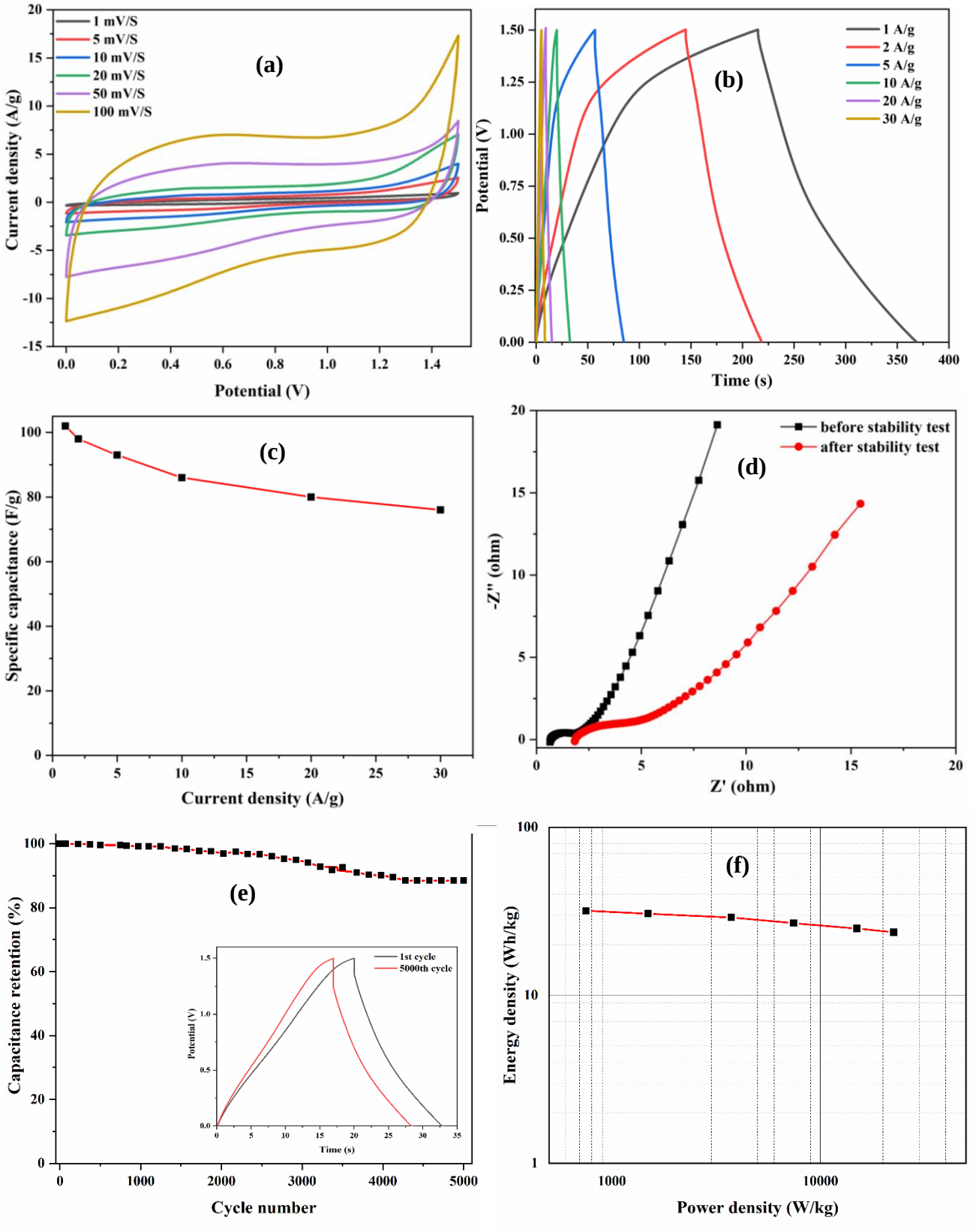

Fig.4.9 (a) CV of h-BN/rGO/CdS@PPy//AC at different scan rates. (b) GCD of h-BN/rGO/CdS@PPy//AC at different current densities. (c) Plot of Specific capacitance Vs. Current density. (d) EIS of h-BN/rGO/CdS@PPy//AC before and after cycling stability test. (e) Cycling stability of h-BN/rGO/CdS@PPy//AC (inset: 1st and 5000th cycle). (f) Plot of Energy density Vs. Power density.

transfer resistance (Rct) and excellent capacitive behaviour, respectively [78, 79]. The internal resistance (Rs) and charge transfer resistance (Rct) obtained was 0.8Ω and 2.6Ω respectively, which shows the excellent electrical and ionic conductivity of the ASC device [80]. After cycling stability test of the device, the Rs value increased to 1.84Ω and Rct value was 4.2Ω. The increase in the impedance values is due to the structural damage and delamination of material in the electrode after rigorous charge/discharge process in the alkaline media. The cycling stability of h-BN/rGO/CdS@PPy//AC ASC was studied by performing GCD at 10A/g for 5000 cycles. The device retained 88.50% of its initial capacitance after 5000 cycles, as illustrated in Fig.4.9e. Also, the inset first and 5000th GCD wave of stability test. The increased iR drop in the 5000th cycle is due to the reasons described above. The energy density of ASC was calculated as, Es= $\frac{C(\Delta V)^2}{2 * 3.6}$ [81, 82] where, C=specific capacitance (F/g), ΔV=potential (V) where the power density of h-BN/rGO/CdS@PPy sample is determined as Pd= $\frac{E}{\Delta t} * 3600$ [83, 84] where, E=Energy density (Wh/kg), Δt=Time (h). Fig.4.9f shows the energy density and power density from GCD. The highest energy density of 32Wh/kg was obtained at a power density of 750W/kg at 1A/g and energy density was 23.75Wh/kg at a maximum power density of 22.5kW/kg. It was discovered that the energy density and power density of the ASC used in this work were superior to those of several comparable ASCs [2, 12, 85-88].

Table 4.2. Electrochemical performance comparison of various previously reported metal sulphide based composite materials

Sample	**Potential range (V)**	**Specific Capacitance (F/g)**	**Power Density (W/kg)**	**Energy Density (Wh/kg)**
3D-CdS/graphite [12]	0.0-1.6	86 (1 A/g)	800	30.4
Co_3O_4@CdS [2]	0.0-0.8	99 (10mA)	-	40
3D CuS / rGO [85]	0.0-1.5	37.2 (10A/g)	681	16.7
CuS flowers on 3D-graphene [86]	0.0-1.0	32 (1A/g)	450	5

FeS [87]	0.0-2.0	4.62 (0.75mA)	726	2.56
CoS [88]	0.0-1.8	57 (1A/g)	700.12	15.58
h-BN/rGO/CdS@PPy [Present work]	**0.0-1.5**	**102 (1 A/g)**	**750**	**32**

4.4. Conclusion

An h-BN/rGO wrapped CdS/PPy supercapacitor electrode material was developed via a facile hydrothermal process accompanied by chemical oxidative polymerisation mechanism. The band-gap tuned h-BN/rGO superlattice and porous polypyrrole provided better charge transfer pathway between CdS NPs. The h-BN/rGO/CdS@PPy electrode shows very high specific capacitance of 1435F/g in 3M KOH at 1A/g current density. The asymmetric supercapacitor (ASC) fabricated using h-BN/rGO/CdS@PPy//AC presented a specific capacitance of 102F/g at 1A/g and maximum energy density of 32Wh/kg at a power density of 750W/kg. Furthermore, the device retained 88.50% of its initial capacitance after 5000 cycles. The synergetic advantages of high specific capacity, superior mechanical strength and very high conductivity obtained from CdS, h-BN/rGO and PPy respectively promise the h-BN/rGO/CdS@PPy composite as a potential electrode material exhibiting very high specific capacitance and cyclic stability.

Bibliography

[1] Chen, L., Zuo, Y., Zhang, Y. and Gao, Y. MnO2/CdS/N-doped Graphite Nanocomposite for High-Performance Supercapacitors. *Int. J. Electrochem. Sci,* 13:642-654, 2018.

[2] Patil, D. S., Pawar, S. A. and Shin, J. C. Core-shell structure of Co3O4@ CdS for high performance electrochemical supercapacitor. *Chemical Engineering Journal*, 335:693-702, 2018.

[3] Gao, Y., Mi, L., Wei, W., Cui, S., Zheng, Z., Hou, H. and Chen, W. Double metal ions synergistic effect in hierarchical multiple sulfide microflowers for enhanced supercapacitor performance. *ACS applied materials & interfaces,* 7(7):4311-4319, 2015.

[4] Nisha, V., Paravannoor, A., Panoth, D., Manikkoth, S. T., Thulasi, K. M., Palantavida, S. and Vijayan, B. K. CdS nanosheets as electrode materials for all pseudocapacitive asymmetric supercapacitors. *Bulletin of Materials Science,* 44(2):1-7, 2021.

[5] Wang, X., Shi, B., Fang, Y., Rong, F., Huang, F., Que, R. and Shao, M. High capacitance and rate capability of a Ni 3 S 2@ CdS core–shell nanostructure supercapacitor. *Journal of Materials Chemistry A,* 5(15):7165-7172, 2017.

[6] Periasamy, P., Krishnakumar, T., Devarajan, V., Sandhiya, M., Sathish, M. and Chavali, M. Investigation of electrochemical supercapacitor performance of WO3-CdS nanocomposites in 1 M H2SO4 electrolyte prepared by microwave-assisted method. *Materials Letters,* 274:127998, 2020.

[7] Xu, P., Liu, J., Yan, P., Miao, C., Ye, K., Cheng, K., Yin, J., Cao, D., Li, K. and Wang, G. Preparation of porous cadmium sulphide on nickel foam: a novel electrode material with excellent supercapacitor performance. *Journal of Materials Chemistry A,* 4(13):4920-4928, 2016.

[8] Saha, D., Li, Y., Bi, Z., Chen, J., Keum, J. K., Hensley, D. K., Grappe, H. A., Meyer III, H. M., Dai, S. and Paranthaman, M. P. Studies on supercapacitor electrode material from activated lignin-derived mesoporous carbon. *Langmuir,* 30(3):900-910, 2014.

[9] Zheng, S., Li, Q., Xue, H., Pang, H. and Xu, Q. A highly alkaline-stable metal oxide@ metal–organic framework composite for high-performance electrochemical energy storage. *National science review,* 7(2):305-314, 2020.

[10] Panicker, N. J., Das, J. and Sahu, P. Synthesis of highly oxidized graphene (HOG) by using HNO3 and KMnO4 as oxidizing agents. *Materials Today: Proceedings,* 2020.

[11] Zhang, X., Ge, X., Sun, S., Qu, Y., Chi, W., Chen, C. and Lü, W. Morphological control of RGO/CdS hydrogels for energy storage. *CrystEngComm,* 18(7):1090-1095, 2016.

[12] Chen, L., Zuo, Y., Zhang, Y. and Gao, Y. Cadmium sulfide anchored in three-dimensional graphite cage for high performance supercapacitors. *Applied Physics Letters*, 112(22):223901, 2018.

[13] Shown, I., Ganguly, A., Chen, L. C. and Chen, K. H. Conducting polymer-based flexible supercapacitor. *Energy Science & Engineering*, 3(1):2-26, 2015.

[14] Wang, Y., Tao, S., An, Y., Wu, S. and Meng, C. Bio-inspired high performance electrochemical supercapacitors based on conducting polymer modified coral-like monolithic carbon. *Journal of Materials Chemistry A*, 1(31):8876-8887, 2013.

[15] Biswas, S. and Drzal, L. T. Multilayered nanoarchitecture of graphene nanosheets and polypyrrole nanowires for high performance supercapacitor electrodes. *Chemistry of Materials*, 22(20):5667-5671, 2010.

[16] Xu, J., Wang, D., Yuan, Y., Wei, W., Duan, L., Wang, L., Bao, H. and Xu, W. Polypyrrole/reduced graphene oxide coated fabric electrodes for supercapacitor application. *Organic Electronics*, 24:153-159, 2015.

[17] Xu, S., Hao, H., Chen, Y., Li, W., Shen, W., Shearing, P. R., Brett, D. J. and He, G. Flexible all-solid-state supercapacitors based on PPy/rGO nanocomposite on cotton fabric. *Nanotechnology*, 32(30):305401, 2021.

[18] Gao, G., Gao, W., Cannuccia, E., Taha-Tijerina, J., Balicas, L., Mathkar, A., Narayanan, T., Liu, Z., Gupta, B. K. and Peng, J. Artificially stacked atomic layers: toward new van der Waals solids. *Nano letters*, 12(7):3518-3525, 2012.

[19] Saha, S., Jana, M., Samanta, P., Murmu, N. C., Kim, N. H., Kuila, T. and Lee, J. H. Investigation of band structure and electrochemical properties of h-BN/rGO composites for asymmetric supercapacitor applications. *Materials Chemistry and Physics*, 190:153-165, 2017.

[20] Murugadoss, G., Thangamuthu, R., Jayavel, R. and Kumar, M. R. Narrow with tunable optical band gap of CdS based core shell nanoparticles: Applications in pollutant degradation and solar cells. *Journal of Luminescence*, 165:30-39, 2015.

[21] Zhai, L., Liu, Z., Li, C., Qu, X., Zhang, Q., Li, G., Zhang, X. and Abdel-Magid, B. Cyanate ester resin based composites with high toughness and thermal conductivity. *RSC advances*, 9(10):5722-5730, 2019.

[22] Shaybanizadeh, S. and Chermahini, A. N. Fabricating boron nitride nanosheets from hexagonal BN in water solution by a combined sonication and thermal-assisted hydrolysis method. *Ceramics International*, 47(8):11122-11128, 2021.

[23] Cho, G., Fung, B. M., Glatzhofer, D. T., Lee, J.-S. and Shul, Y.-G. Preparation and characterization of polypyrrole-coated nanosized novel ceramics. *Langmuir,* 17(2):456-461, 2001.

[24] Fan, X., Yang, Z. and He, N. Hierarchical nanostructured polypyrrole/graphene composites as supercapacitor electrode. *RSC advances,* 5(20):15096-15102, 2015.

[25] López-García, F., Canché-Escamilla, G., Ocampo-Flores, A., Roquero-Tejeda, P. and Ordóñez, L. Controlled size nano-polypyrrole synthetized in micro-emulsions as PT support for the ethanol electro-oxidation reaction. *International Journal of Electrochemical Science,* 8(3):3794-3813, 2013.

[26] Qu, B., Xu, Y.-T., Lin, S.-j., Zheng, Y.-F. and Dai, L.-Z. Fabrication of Pt nanoparticles decorated PPy–MWNTs composites and their electrocatalytic activity for methanol oxidation. *Synthetic Metals,* 160(7-8):732-742, 2010.

[27] Habibi, M. H. and Rahmati, M. H. Fabrication and characterization of ZnO@ CdS core–shell nanostructure using acetate precursors: XRD, FESEM, DRS, FTIR studies and effects of cadmium ion concentration on band gap. *Spectrochimica Acta Part A: Molecular and Biomolecular Spectroscopy,* 133:13-18, 2014.

[28] Mondal, G., Acharjya, M., Santra, A., Bera, P., Jana, S., Pramanik, N. C., Mondal, A. and Bera, P. A new pyrazolyl dithioate function in the precursor for the shape controlled growth of CdS nanocrystals: optical and photocatalytic activities. *New Journal of Chemistry,* 39(12):9487-9496, 2015.

[29] Zhou, H., Han, G., Xiao, Y., Chang, Y. and Zhai, H.-J. Facile preparation of polypyrrole/graphene oxide nanocomposites with large areal capacitance using electrochemical codeposition for supercapacitors. *Journal of Power Sources,* 263:259-267, 2014.

[30] Panicker, N. J. and Sahu, P. P. Green reduction of graphene oxide using phytochemicals extracted from Pomelo Grandis and Tamarindus indica and its supercapacitor applications. *Journal of Materials Science: Materials in Electronics*:1-14, 2021.

[31] Maity, C. K., Hatui, G., Sahoo, S., Saren, P. and Nayak, G. C. Boron nitride based ternary nanocomposites with different carbonaceous materials decorated by polyaniline for supercapacitor application. *ChemistrySelect,* 4(13):3672-3680, 2019.

[32] Yuan, S., Toury, B., Benayoun, S., Chiriac, R., Gombault, F., Journet, C. and Brioude, A. Low-temperature synthesis of highly crystallized hexagonal boron nitride sheets with Li3N as additive agent. *European Journal of Inorganic Chemistry,* 2014(32):5507-5513, 2014.

[33] Lee, H., Issam, A., Belmahi, M., Assouar, M., Rinnert, H. and Alnot, M. Synthesis and characterizations of bare CdS nanocrystals using chemical precipitation method for photoluminescence application. *Journal of Nanomaterials*, 2009, 2009.

[34] Ahmad, N., Sultana, S., Sabir, S. and Khan, M. Z. Exploring the visible light driven photocatalysis by reduced graphene oxide supported Ppy/CdS nanocomposites for the degradation of organic pollutants. *Journal of Photochemistry and Photobiology A: Chemistry,* 386:112129, 2020.

[35] Kudin, K. N., Ozbas, B., Schniepp, H. C., Prud'Homme, R. K., Aksay, I. A. and Car, R. Raman spectra of graphite oxide and functionalized graphene sheets. *Nano letters,* 8(1):36-41, 2008.

[36] Gautam, M., Shi, Z. and Jayatissa, A. H. Graphene films as transparent electrodes for photovoltaic devices based on cadmium sulfide thin films. *Solar Energy Materials and Solar Cells,* 163:1-8, 2017.

[37] Ahmed, K., Dahal, R., Weltz, A., Lu, J.-Q., Danon, Y. and Bhat, I. Growth of hexagonal boron nitride on (111) Si for deep UV photonics and thermal neutron detection. *Applied Physics Letters,* 109(11):113501, 2016.

[38] Cheng, Q., He, Y., Pavlinek, V., Li, C. and Saha, P. Surfactant-assisted polypyrrole/titanate composite nanofibers: Morphology, structure and electrical properties. *Synthetic Metals,* 158(21-24):953-957, 2008.

[39] Yang, S., Shen, C., Liang, Y., Tong, H., He, W., Shi, X., Zhang, X. and Gao, H.-j. Graphene nanosheets-polypyrrole hybrid material as a highly active catalyst support for formic acid electro-oxidation. *Nanoscale,* 3(8):3277-3284, 2011.

[40] Saha, S., Jana, M., Khanra, P., Samanta, P., Koo, H., Murmu, N. C. and Kuila, T. Band gap engineering of boron nitride by graphene and its application as positive electrode material in asymmetric supercapacitor device. *ACS applied materials & interfaces,* 7(26):14211-14222, 2015.

[41] Maity, C. K., Santra, D. K., Verma, K., Sahoo, S., Cotts, S., Akinwande, D., Berry, V. and Nayak, G. C. Induced conducting energy-levels in a boron nitride nano-framework for asymmetric supercapacitors in high charge-mobility ionic electrolytes. *Composites Part B: Engineering,* 212:108728, 2021.

[42] Ci, L., Song, L., Jin, C., Jariwala, D., Wu, D., Li, Y., Srivastava, A., Wang, Z., Storr, K. and Balicas, L. Atomic layers of hybridized boron nitride and graphene domains. *Nature materials,* 9(5):430-435, 2010.

[43] Mussa, Y., Ahmed, F., Arsalan, M. and Alsharaeh, E. Two dimensional (2D) reduced graphene oxide (RGO)/hexagonal boron nitride (h-BN) based nanocomposites as anodes for high temperature rechargeable lithium-ion batteries. *Scientific reports,* 10(1):1-13, 2020.

[44] Yue, X., Yi, S., Wang, R., Zhang, Z. and Qiu, S. Cadmium sulfide and nickel synergetic co-catalysts supported on graphitic carbon nitride for visible-light-driven photocatalytic hydrogen evolution. *Scientific reports,* 6(1):1-9, 2016.

[45] Feng, M., Lu, W., Zhou, Y., Zhen, R., He, H., Wang, Y. and Li, C. Synthesis of polypyrrole/nitrogen-doped porous carbon matrix composite as the electrode material for supercapacitors. *Scientific reports,* 10(1):1-12, 2020.

[46] White, R. J., Budarin, V., Luque, R., Clark, J. H. and Macquarrie, D. J. Tuneable porous carbonaceous materials from renewable resources. *Chemical Society Reviews,* 38(12):3401-3418, 2009.

[47] Fan, M., Wu, J., Yuan, J., Deng, L., Zhong, N., He, L., Cui, J., Wang, Z., Behera, S. K. and Zhang, C. Doping nanoscale graphene domains improves magnetism in hexagonal boron nitride. *Advanced Materials,* 31(12):1805778, 2019.

[48] Saha, S., Samanta, P., Murmu, N. C., Banerjee, A., Ganesh, R. S., Inokawa, H. and Kuila, T. Modified electrochemical charge storage properties of h-BN/rGO superlattice through the transition from n to p type semiconductor by fluorine doping. *Chemical Engineering Journal,* 339:334-345, 2018.

[49] Oraon, R., De Adhikari, A., Tiwari, S. K., Sahu, T. S. and Nayak, G. C. Fabrication of nanoclay based graphene/polypyrrole nanocomposite: An efficient ternary electrode material for high performance supercapacitor. *Applied Clay Science,* 118:231-238, 2015.

[50] Zhang, J. and Zhao, X. Conducting polymers directly coated on reduced graphene oxide sheets as high-performance supercapacitor electrodes. *The Journal of Physical Chemistry C,* 116(9):5420-5426, 2012.

[51] Sahoo, S., Kumar, R., Joanni, E., Singh, R. K. and Shim, J.-J. Advances in pseudocapacitive and battery-like electrode materials for high performance supercapacitors. *Journal of Materials Chemistry A,* 10(25):13190-13240, 2022.

[52] Kumar, R., Sahoo, S., Joanni, E. and Singh, R. K. A review on the current research on microwave processing techniques applied to graphene-based supercapacitor electrodes: An emerging approach beyond conventional heating. *Journal of Energy Chemistry,* 2022.

[53] Shao, Y., El-Kady, M. F., Wang, L. J., Zhang, Q., Li, Y., Wang, H., Mousavi, M. F. and Kaner, R. B. Graphene-based materials for flexible supercapacitors. *Chemical Society Reviews,* 44(11):3639-3665, 2015.

[54] Mazov, I., Kuznetsov, V., Romanenko, A., Suslyaev, V. and Hu, N. Properties of MWNT-Containing Polymer Composite Materials Depending on Their Structure. in Composites and Their Properties. 2012, InTech.

[55] Patil, I. M., Kapse, S., Parse, H., Thapa, R., Andersson, G. and Kakade, B. 2D/3D heterostructure of h-BN/reduced graphite oxide as a remarkable electrode Material for supercapacitor. *Journal of Power Sources,* 479:229092, 2020.

[56] Yan, Y., Lin, J., Cao, J., Guo, S., Zheng, X., Feng, J. and Qi, J. Activating and optimizing the activity of NiCoP nanosheets for electrocatalytic alkaline water splitting through the V doping effect enhanced by P vacancies. *Journal of Materials Chemistry A,* 7(42):24486-24492, 2019.

[57] Yan, D., Li, Y., Liu, Y., Zhuo, R., Geng, B., Wu, Z., Wang, J., Ren, P. and Yan, P. Design and influence of mass ratio on supercapacitive properties of ternary electrode material reduced graphene oxide@ MnO2@ poly (3, 4-ethylenedioxythiophene)-poly (styrene sulfonate). *Electrochimica Acta,* 169:317-325, 2015.

[58] Cheng, Y., Guo, X., Xue, Y. and Pang, H. Controllable synthesis of a flower-like superstructure of nickel metal-organic phosphate and its derivatives for supercapacitors. *Applied Materials Today,* 23:101048, 2021.

[59] Yan, Y., Liu, J., Huang, K., Qi, J., Qiao, L., Zheng, X. and Cai, W. A fast micro–nano liquid layer induced construction of scaled-up oxyhydroxide based electrocatalysts for alkaline water splitting. *Journal of Materials Chemistry A*, 9(47):26777-26787, 2021.

[60] Pawar, S. A., Patil, D. S., Shin, J. C. and Kim, H. J. Enhanced battery-type supercapacitor performance based on composite structure of nickel cobaltite and cadmium sulfide. *Journal of Electroanalytical Chemistry,* 873:114370, 2020.

[61] Yan, Y., Lin, J., Xu, T., Liu, B., Huang, K., Qiao, L., Liu, S., Cao, J., Jun, S. C. and Yamauchi, Y. Atomic-Level Platinum Filling into Ni-Vacancies of Dual-Deficient NiO for Boosting Electrocatalytic Hydrogen Evolution. *Advanced Energy Materials*:2200434, 2022.

[62] Jing, Q., Li, W., Wang, J., Chen, X. and Pang, H. Calcination activation of three-dimensional cobalt organic phosphate nanoflake assemblies for supercapacitors. *Inorganic Chemistry Frontiers,* 8(18):4222-4229, 2021.

[63] He, Y., Zhang, X., Wang, J., Sui, Y., Qi, J., Chen, Z., Zhang, P., Chen, C. and Liu, W. Constructing Co (OH) F nanorods@ NiCo-LDH nanocages derived from ZIF-67 for high-performance supercapacitors. *Advanced Materials Interfaces,* 8(17):2100642, 2021.

[64] He, Y., Liu, D., Zhao, H., Wang, J., Sui, Y., Qi, J., Chen, Z., Zhang, P., Chen, C. and Zhuang, D. Carbon-coated NiMn layered double hydroxides/Ni3S2 nanocomposite for high performance supercapacitors. *Journal of Energy Storage*, 41:103003, 2021.

[65] Liu, S., Yin, Y., Ni, D., San Hui, K., Ma, M., Park, S., Hui, K. N., Ouyang, C.-Y. and Jun, S. C. New insight into the effect of fluorine doping and oxygen vacancies on electrochemical performance of Co2MnO4 for flexible quasi-solid-state asymmetric supercapacitors. *Energy Storage Materials*, 22:384-396, 2019.

[66] Zhang, X., Wang, J., Sui, Y., Wei, F., Qi, J., Meng, Q., He, Y. and Zhuang, D. Hierarchical nickel–cobalt phosphide/phosphate/carbon nanosheets for high-performance supercapacitors. *ACS Applied Nano Materials*, 3(12):11945-11954, 2020.

[67] Liu, D., Li, S., He, Y., Liu, C., Li, Q., Sui, Y., Qi, J., Zhang, P., Chen, C. and Chen, Z. Co (OH) F@ CoP/CC core-shell nanoarrays for high-performance supercapacitors. *Journal of Energy Storage*, 55:105417, 2022.

[68] Purty, B., Choudhary, R., Biswas, A. and Udayabhanu, G. Potentially enlarged supercapacitive values for CdS-PPY decorated rGO nanocomposites as electrode materials. *Materials Chemistry and Physics*, 216:213-222, 2018.

[69] Shiri, H. M. and Ehsani, A. Pulse electrosynthesis of novel wormlike gadolinium oxide nanostructure and its nanocomposite with conjugated electroactive polymer as a hybrid and high efficient electrode material for energy storage device. *Journal of colloid and interface science*, 484:70-76, 2016.

[70] Yan, Y., Lin, J., Liu, T., Liu, B., Wang, B., Qiao, L., Tu, J., Cao, J. and Qi, J. Corrosion behavior of stainless steel-tungsten carbide joints brazed with AgCuX (X= In, Ti) alloys. *Corrosion Science*, 200:110231, 2022.

[71] Liu, S., Ni, D., Li, H.-F., Hui, K. N., Ouyang, C.-Y. and Jun, S. C. Effect of cation substitution on the pseudocapacitive performance of spinel cobaltite MCo 2 O 4 (M= Mn, Ni, Cu, and Co). *Journal of Materials Chemistry A*, 6(23):10674-10685, 2018.

[72] Li, L., San Hui, K., Hui, K. N. and Cho, Y.-R. Ultrathin petal-like NiAl layered double oxide/sulfide composites as an advanced electrode for high-performance asymmetric supercapacitors. *Journal of Materials Chemistry A*, 5(37):19687-19696, 2017.

[73] Liu, S., Hui, K. S. and Hui, K. N. 1 D hierarchical MnCo2O4 nanowire@ MnO2 sheet core–shell arrays on graphite paper as superior electrodes for asymmetric supercapacitors. *ChemNanoMat*, 1(8):593-602, 2015.

[74] Sk, M. M. and Yue, C. Y. Synthesis of polyaniline nanotubes using the self-assembly behavior of vitamin C: a mechanistic study and application in electrochemical supercapacitors. *Journal of Materials Chemistry A*, 2(8):2830-2838, 2014.

[75] Mohammadi, A., Arsalani, N., Tabrizi, A. G., Moosavifard, S. E., Naqshbandi, Z. and Ghadimi, L. S. Engineering rGO-CNT wrapped Co3S4 nanocomposites for high-performance asymmetric supercapacitors. *Chemical Engineering Journal*, 334:66-80, 2018.

[76] Ghosh, D. and Das, C. K. Hydrothermal growth of hierarchical Ni3S2 and Co3S4 on a reduced graphene oxide hydrogel@ Ni foam: a high-energy-density aqueous asymmetric supercapacitor. *ACS applied materials & interfaces*, 7(2):1122-1131, 2015.

[77] Li, J., Zou, Y., Jin, L., Xu, F., Sun, L. and Xiang, C. Polydopamine-assisted NiMoO4 nanorods anchored on graphene as an electrode material for supercapacitor applications. *Journal of Energy Storage*, 50:104639, 2022.

[78] Zou, Y., Zhang, X., Liang, J., Xiang, C., Chu, H., Zhang, H., Xu, F. and Sun, L. Encapsulation of hollow Cu2O nanocubes with Co3O4 on porous carbon for energy-storage devices. *Journal of Materials Science & Technology*, 55:182-189, 2020.

[79] Xu, J., Liang, J., Zou, Y., Xu, F., Chen, Q., Xiang, C., Zhang, J. and Sun, L. Layer-by-layer self-assembled GO-MoS2Co3O4 three-dimensional conducting network for high-performance supercapacitors. *Journal of Energy Storage*, 43:103195, 2021.

[80] Liu, Y., Xiang, C., Chu, H., Qiu, S., McLeod, J., She, Z., Xu, F., Sun, L. and Zou, Y. Binary Co–Ni oxide nanoparticle-loaded hierarchical graphitic porous carbon for high-performance supercapacitors. *Journal of Materials Science & Technology*, 37:135-142, 2020.

[81] Li, W., Guo, X., Geng, P., Du, M., Jing, Q., Chen, X., Zhang, G., Li, H., Xu, Q. and Braunstein, P. Rational Design and General Synthesis of Multimetallic Metal–Organic Framework Nano-Octahedra for Enhanced Li–S Battery. *Advanced Materials*, 33(45):2105163, 2021.

[82] Zhang, X., Zhang, R., Xiang, C., Liu, Y., Zou, Y., Chu, H., Qiu, S., Xu, F. and Sun, L. Polydopamine-assisted formation of Co3O4-nanocube-anchored reduced graphene oxide composite for high-performance supercapacitors. *Ceramics International*, 45(11):13894-13902, 2019.

[83] Bai, Y., Liu, C., Chen, T., Li, W., Zheng, S., Pi, Y., Luo, Y. and Pang, H. MXene-copper/cobalt hybrids via lewis acidic molten salts etching for high performance symmetric supercapacitors. *Angewandte Chemie*, 133(48):25522-25526, 2021.

[84] Xiang, C., Wang, Q., Zou, Y., Huang, P., Chu, H., Qiu, S., Xu, F. and Sun, L. Simple synthesis of graphene-doped flower-like cobalt–nickel–tungsten–boron oxides with self-

oxidation for high-performance supercapacitors. *Journal of Materials Chemistry A,* 5(20):9907-9916, 2017.

[85] Cui, Y., Zhang, J., Li, G., Sun, Y., Zhang, G. and Zheng, W. Ionic liquid-assisted synthesis of rGO wrapped three-dimensional CuS ordered nanoerythrocytes with enhanced performance for asymmetric supercapacitors. *Chemical Engineering Journal,* 325:424-432, 2017.

[86] Tian, Z., Dou, H., Zhang, B., Fan, W. and Wang, X. Three-dimensional graphene combined with hierarchical CuS for the design of flexible solid-state supercapacitors. *Electrochimica Acta,* 237:109-118, 2017.

[87] Karade, S. S., Dwivedi, P., Majumder, S., Pandit, B. and Sankapal, B. R. First report on a FeS-based 2 V operating flexible solid-state symmetric supercapacitor device. *Sustainable Energy & Fuels,* 1(6):1366-1375, 2017.

[88] Ashok Kumar, K., Pandurangan, A., Arumugam, S. and Sathiskumar, M. Effect of bi-functional hierarchical flower-like CoS nanostructure on its interfacial charge transport kinetics, magnetic and electrochemical behaviors for supercapacitor and DSSC applications. *Scientific reports,* 9(1):1-16, 2019.